Surrogate-Based Low-Boom Low-Drag Nose Design for the JAXA S4 Supersonic Airliner

Jochen Kirz *

German Aerospace Center (DLR), Institute of Aerodynamics and Flow Technology,
Lilienthalplatz 7, 38108 Braunschweig, Germany

Robust low-boom low-drag design methods were developed within a trilateral collaboration between JAXA, ONERA and DLR on the en-route noise of supersonic civil aircraft. In this paper the nose of the JAXA S4.1.3.4[th] supersonic low-boom airliner is optimized using a surrogate-based optimization method. The optimization process includes near-field Euler simulations with the DLR TAU code and a propagation algorithm developed at ONERA based on the TRAPS code. The maximum level of perceived loudness for different off-track angles as well as the drag coefficient are used as objective functions for a multi-objective optimization. A reduction of the off-track noise by $2\,\mathrm{dB}\,\mathrm{PL}$ as well as a small drag reduction can be achieved by the nose optimization. The impact on the pitching moment is analyzed.

Nomenclature

C_D	= Drag coefficient		direction in m
C_L	= Lift coefficient	X	= Distance from nose in freestream direction
$C_m, pitch$	= Pitching moment coefficient		in m
L	= Body length in m	X_N	= Distance from nose in freestream direction
M	= Mach number		normalized by Mach angle
p	= Static pressure in Pa	∞	= Freestream value
PL	= Perceived loudness in dB	μ	= Mach angle in degree
R	= Distance from body centerline in radial	$\Delta p / p_\infty$	= Normalized pressure difference

I. Introduction

The sonic boom remains a major challenge in the development and potential certification of supersonic civil aircraft. In order to contribute to the international discussion about sonic boom noise certification standards a trilateral collaboration between JAXA, ONERA and DLR was initiated in 2017. Two objectives of the collaboration were the accurate sonic-boom prediction and the robust low-boom design in the whole boom carpet. A detailed description of the collaboration is presented by Ueno and Makino in Ref. [1].

The AIAA Sonic Boom Prediction Workshop (SBPW) was established to assess the state of the art for predicting near-field pressure signatures, propagated ground signatures and ground loudness levels needed for accurate and reliable sonic boom prediction with numerical methods. The second AIAA Sonic Boom Prediction Workshop (SBPW2) took place in January of 2017 and covered both, the state-of-the-art for predicting near field sonic boom signatures with CFD [2], as well as the propagation of the near-field pressure signatures to the ground [3]. The international participation in SBPW2 showed that uncertainties remain when solving flow fields for complex geometries with an integrated engine and CFD engine boundary conditions. The third AIAA Sonic Boom Prediction Workshop (SBPW3) addressed these topics [4–6].

Within WP1 of the trilateral collaboration the partners participated in the SBPWs and showed that the available numerical methods are able to accurately calculate pressure signatures in the near-field of the geometry and on the ground [7–10]. The best-practices for numerical simulation of the near-field developed during those studies are applied in this paper.

The robust low-boom design is addressed in WP3 of the collaboration [1] which was finished in December 2020. DLR initially developed the tools and methods for the surrogate-based low-boom low-drag design using simplified

---

*Research Scientist, Transport Aircraft Branch, AIAA member

1

geometries like an axi-symmetric body [11] and a wing-body configuration [12]. A method for the design of the nose of a complex low-boom supersonic aircraft geometry was developed by DLR within the RUMBLE (RegUlation and norM for low sonic Boom LEvels) EC-project. However, no propagation algorithm was available for DLR within the RUMBLE project and a target near-field signature had to be used as an objective. This study showed the importance of using the propagation algorithm in the loop, which will be applied in this paper.

II. Optimization Setup

The optimization process is based on the numerical simulation of the sonic boom, which can be divided into three parts. Firstly, computational fluid dynamics (CFD) is used to calculate the near-field pressure signature at a distance of several body lengths to the geometry, as shown in Fig. 1. This pressure signature is used as an input for a propagation algorithm, which simulates the propagation through the atmosphere and calculates the pressure signature on the ground. Finally, the loudness is calculated from the ground pressure signature. This section describes the programs and tools used for the simulations and the optimization in detail.
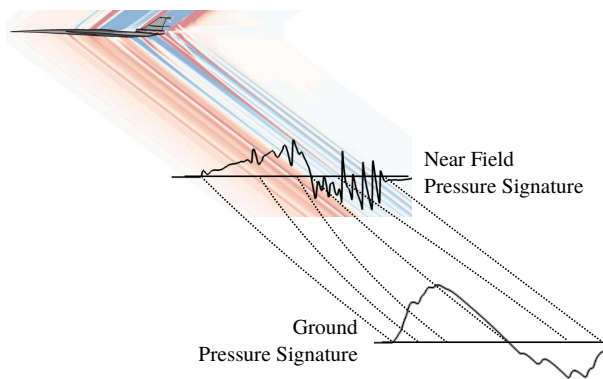

Fig. 1 Prediction of the sonic boom.

A. Geometry

The S4.1.3.4th geometry was provided by JAXA, as shown in Fig. 2. It is a twin engine airliner designed for 36-50 passengers, a range of 3500 NM, and a cruise flight with a Mach number of $M = 1.6$ at a maximum of 49,000 ft cruise altitude. The body length is $L = 64$ m and the MTOM is 68 tons. A more detailed description of the geometry and further studies of the low-boom design can be found in Refs. [1, 13, 14]. For this optimization the engines were neglected in order to decrease the required CPU time for each iteration. This has an impact on the overall loudness of the sonic boom but the relative trends during the nose optimization should not be affected.
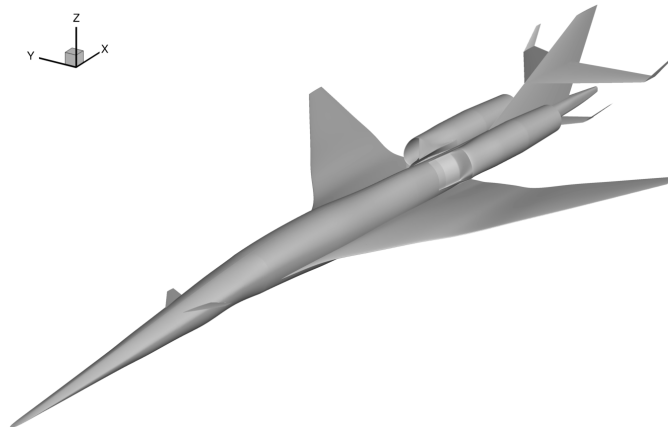

Fig. 2 JAXA S4.1.3.4 geometry.

The initial geometry used for the optimization in this study is derived from the S4.1.3.4[th] case. A fully parametric CATIA model was developed based on the provided geometry files of the S4.1.3.4[th] and an enhanced version of the CAD model for universal aircraft geometries developed at DLR by Ronzheimer [15]. The universal CAD model primarily utilizes B-splines for the construction of the aircraft parts like fuselage sections and airfoils. The B-spline parameterization of the fuselage prevents wavy panels and ensures that the resulting geometries are curvature constant, which is important for the shock and expansion pattern of supersonic bodies. An overview of the parametric CAD model of the fuselage is shown in Fig 3.

In total, nine parametric sections are used for the optimization, specified by their width and height. The spacing of the sections is reduced by half in the vicinity of the canard. In the front part of the nose the upper curve at the symmetry plane is simplified by a straight line. This line is not modified during the optimization in order not to influence cockpit vision and reduce the number of design parameters. The number of design parameters is further reduced by only specifying and varying the width at six out of the nine sections (1, 3, 5, 7, 8, and 9). For all sections the height of the sections relative to the upper curve is varied.

The cross-sectional shape of the sections relative to their width and height is not changed during the optimization. A detailed description of the parameterization of the section shapes can be found in Ref. [16]. In addition to the width and height of the sections the tangential angle at the tip of the nose is an important design parameter. This sums up to a total of 16 design parameters that were used in the optimization.
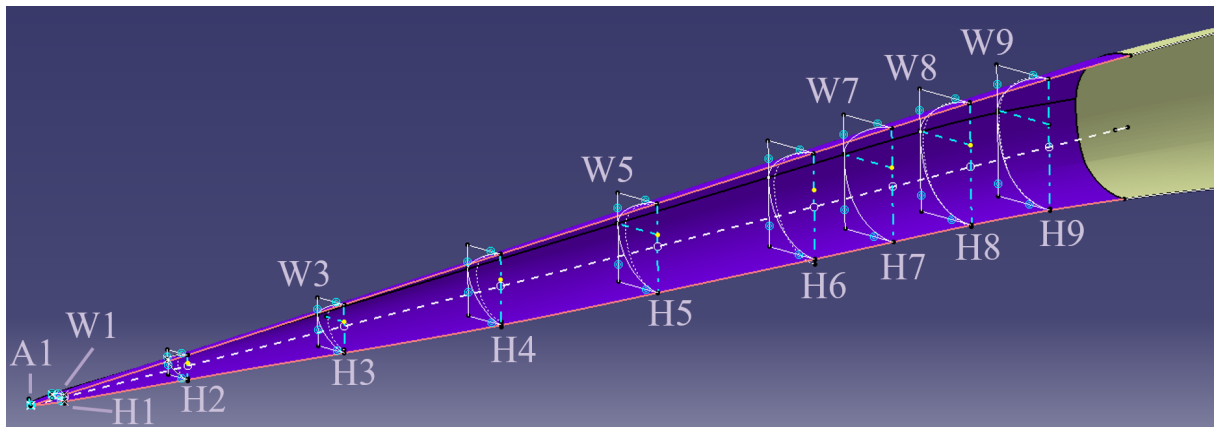
a) Side view.
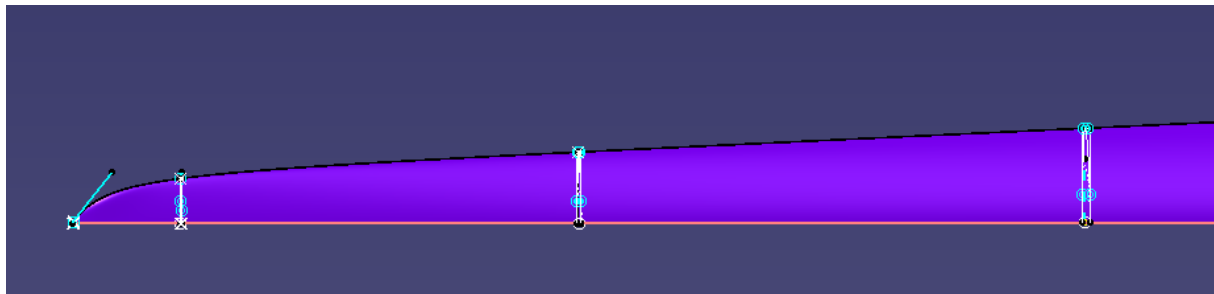
b) Top view (zoomed).

Fig. 3   Parametric CAD model of the S4.1.3.4[th] nose.

B. Grid Setup

The grid setup is similar to the grid setup described in reference [7] for the C25D case of SBPW2. In contrast to the grids for the workshop, in this case a modular grid generation approach is used to easily replace geometries during the optimization process and to minimize influences of different grids. Figure 4 shows the mixed-element grid setup of the CENTAUR [17] grids. The inner module highlighted in blue and green is modified during the optimization, whereas the outer (black and orange) part of the geometry and grid remains constant. This decreases the CPU time required for

3

the grid generation process and also decreases influence of the grids on the optimization result.

The near-field consists of unstructured tetrahedra and the farfield is fully structured. All cells in the farfield are aligned to the Mach cone. An elliptical cross section of the inner part is used to decrease the size of unstructured and unaligned elements. The grid extends to seven body lengths in radial direction. The surface resolution is sufficiently fine to ensure a constant pressure signature at all off-track angles and to prevent unphysical shocks and expansions due to the surface discretization. When normalizing the distance from the nose in freestream direction X by the Mach angle μ

$$X_N = X - \frac{R}{\tan(\mu)} = X - \frac{R}{\tan(\sin^{-1}(\frac{1}{M}))} \tag{1}$$

the general resolution of the grid is 500 nodes in streamwise direction for $0 < X_N/L < 1.2$, while the nose is refined and parts of the grid upstream of the Mach cone are increasingly coarse. The structured farfield has 100 nodes in radial direction. Cells below the geometry are uniformly distributed in circumferential direction, while the grid density decreases above the geometry.

In order to keep the unstructured core part of the grid as small as possible the angle of attack is fixed at $0°$ for the grid generation process. It is changed afterwards to $4°$ using the grid deformation technique. The radius of influence for the grid deformation is selected to be half the length of the aircraft. As a consequence of this deformation a misalignment of the collar grid compared to the Mach cone is induced, as can be seen in Figure 4a). The misalignment of the grid becomes maximal near the aft of the aircraft because the reference for the grid deformation is the nose of the aircraft. However, earlier studies with similar changes of the angle of attack showed that the pressure signatures extracted at three to five body lengths are not influenced by the slight misalignment of the grid due to grid deformation [12].

Overall, using the grid deformation improves the quality of the grid compared to a grid with a larger unstructured core part that would be required if the angle of attack would be set geometrically before the grid generation. Since the shape of the nose is optimized and the deformations in the front part of the grid are small, this is a very good compromise.
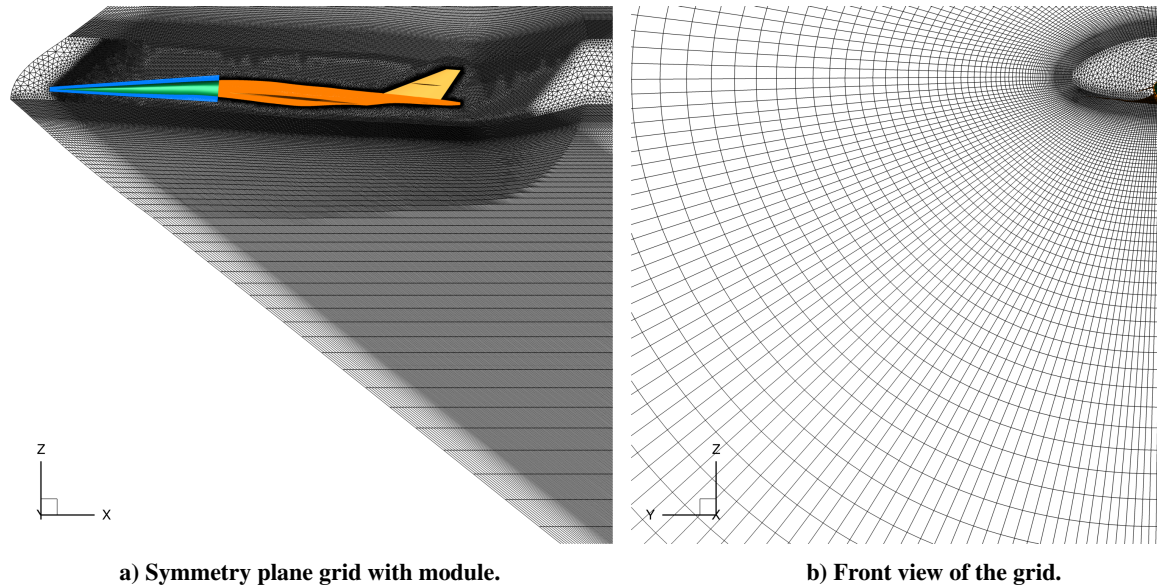

a) Symmetry plane grid with module. b) Front view of the grid.

Fig. 4 Grid setup after grid deformation.

C. Numerical Setup

The near-field CFD simulations are performed with the DLR TAU code [18], which is based on an unstructured finite-volume approach for solving the Euler or Reynolds-averaged Navier-Stokes (RANS) equations on hybrid grids. The second-order accurate AUSMDV upwind scheme [19] is applied for the spatial discretization of the convective fluxes and an implicit lower upper symmetric Gauss Seidel scheme is used for time stepping. The gradients are computed using a Green Gauss approach. The limiting strategy by Barth and Jesperson [20] is used to stabilize the numerical scheme. All calculations performed for this study are Euler simulations without multigrid acceleration.

The near-field pressure distributions are extracted from the CFD solution for a cylinder at three and five body lengths distance to the body ($R/L = 5$ and $R/L = 3$). The pressure signatures extracted at $R/L = 5$ are used as input for the propagation algorithm. For this study, a tool based on the TRAPS code [21] is used. The version provided by the French national aerospace research center (ONERA) has been developed and validated against several experimental data including Jericho-Carton tests using a Mirage IV [22]. The perceived loudness is calculated with the loudness metrics tool pyBoomMetrics, which was also developed at ONERA.

D. Optimization Process

The novel framework Powerful Optimization Tools with Surrogate Modeling (POT) was developed at the German Aerospace Center (DLR) by Wilke [23]. In this study it is used as a framework for surrogate modeling and optimization. It provides various algorithms to build surrogate models for single and multi-objective optimizations and possibilities to tune the hyperparameters of Kriging surrogate models [24]. It offers an interface to run the design of experiments (DoE) in parallel, which significantly accelerates this time intensive step in the optimization process.

Figure 5 shows the flow chart of the optimization process. In this paper Kriging models of third order are used. Furthermore, the Differential Evolutionary (DE) [25] algorithm for the tuning of the surrogate hyperparameters is applied.

This study is driven by a low-boom low-drag design, so the results presented in the following section are results for multi-objective optimizations including the drag coefficient and maximum level of perceived loudness occurring at any off-track angle the as objectives. The number of points in the DoE is chosen to be ten times the amount of design variables, as suggested in literature [26]. A Centroidal Voronoi tessellatized Latin Hypercube (CVT) [27] is used as sampling technique for the DoE. The pareto confidence [26] is used as a stopping criterion for the multi-objective optimization process.
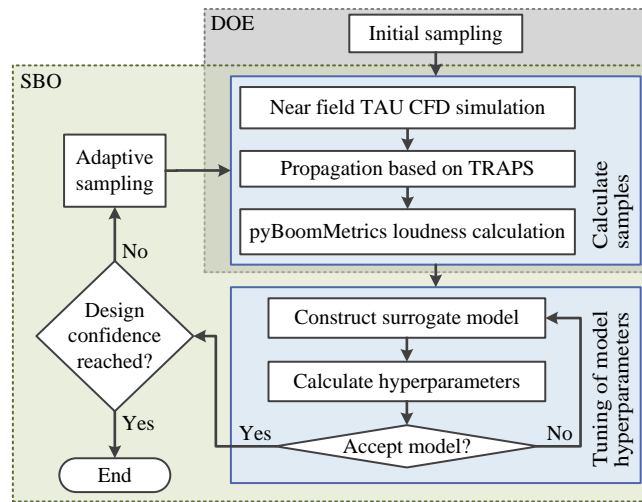

Fig. 5   Flow chart of the optimization process with POT [12].

III. Results

In this section the results of the optimizations are presented and the optimized geometries and the corresponding pressure signatures are analyzed. The results are compared to the baseline S4.1.3.4[th] case. The shown values of the perceived loudness and aerodynamic coefficients are normalized by the corresponding values of the baseline case.

Two separate steps were performed to get a better understanding of the individual design aspects. First, only the front part of the nose was modified. After that, the best design was chosen and the aft part of the nose was further optimized.
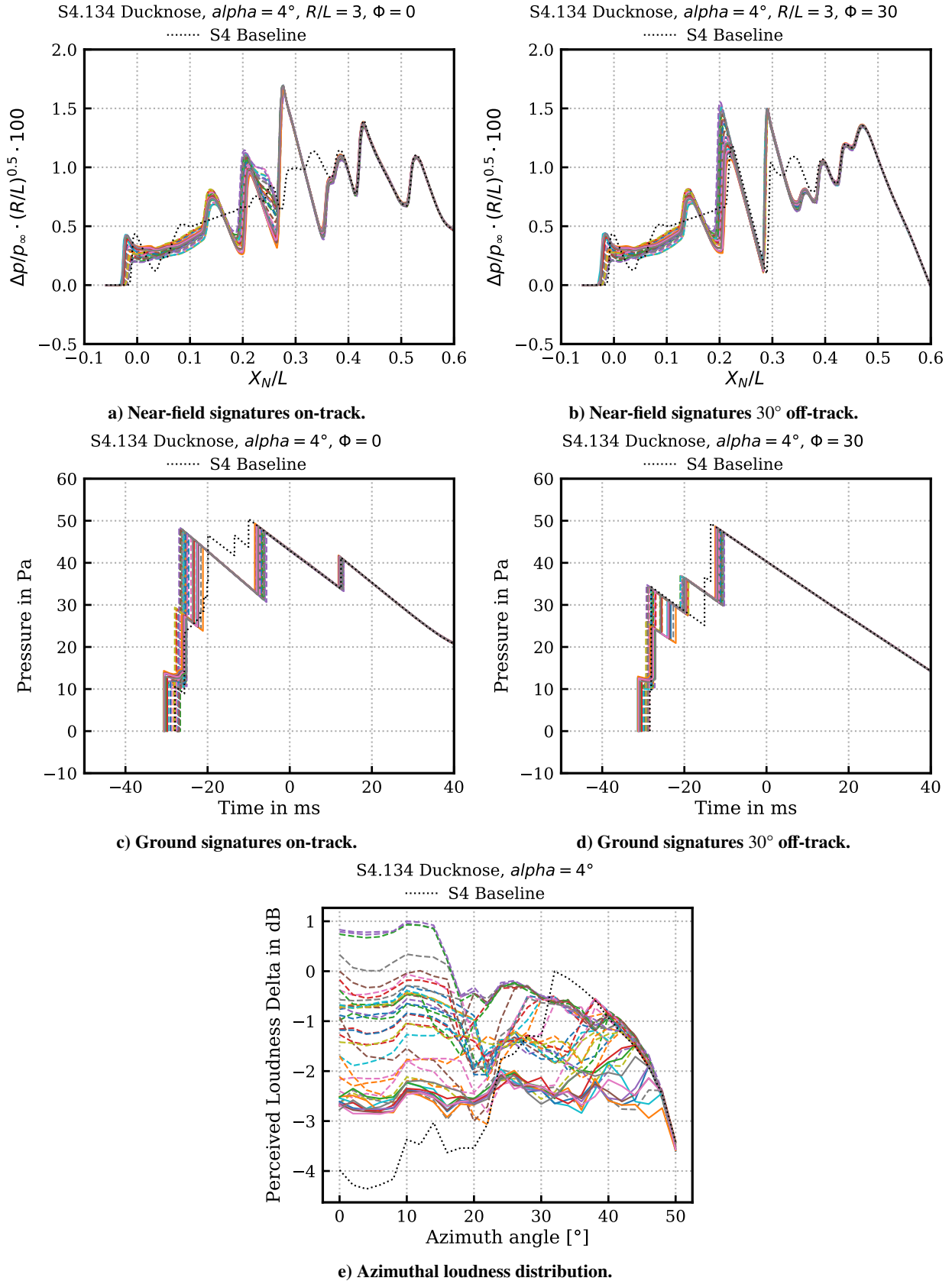
a) Near-field signatures on-track.

b) Near-field signatures 30° **off-track.**

c) Ground signatures on-track.

d) Ground signatures 30° **off-track.**

e) Azimuthal loudness distribution.

Fig. 6   Overview of the simulation results for shape variations at the front part of the nose.

A. Impact of the Shape in the Font Part of the Nose

For the first study only the parameters in the front part (A1, W1-W5, and H1-H5) were varied and an initial setup similar to the baseline geometry was chosen for the parameters in the aft part. An overview of the results of the corresponding simulations is shown in Fig. 6.

Although the geometrical changes are small, the variations in the on-track loudness are up to 4 dB PL, as shown in Fig. 6e). Compared to the baseline case, the selected nose design reduces the off-track loudness significantly. The wide nose causes a stronger shock at the tip of the nose, as shown in Figs. 6a) and 6b). This is beneficial for the loudness because it extends the lengths of the ground signatures and reduces the initial pressure rise for the off-track signatures, as shown in Fig. 6d). The nose tip tangent angle A1 and the first section width W1 had the largest impact on the loudness. The highest reduction of maximum azimuthal sonic boom loudness could be achieved with a tangent nose angle of 41° and a first section width of 400 mm. However, the on-track loudness is increased compared to the baseline because there are strong shocks in the pressure signatures at $X_N/L = 0.3$ corresponding to the aft part of the nose and the canard.

Furthermore, the drag coefficient is increased by two drag counts compared to the baseline geometry. The influence of the performed shape variations in the front part of the nose on the drag coefficient is significantly less than one drag count.

B. Design of the Aft Part of the Nose

A focus of the design of the aft part of the nose was to reduce the drag while maintaining the improvement in loudness achieved by shaping the front part of the nose. For this study the parameters W5-W9 and H5-H9 are varied. After 120 iterations a sufficient pareto confidence was reached and the optimization was stopped, as shown in Fig. 7a). By re-designing the aft part of the nose a reduction of the drag coefficient by roughly one drag count compared to the baseline case was achieved. Compared with the result for the front nose design the drag coefficient was reduced by three drag counts. On the other hand no further reduction in maximum azimuthal loudness was achieved but the on-track loudness was slightly improved.
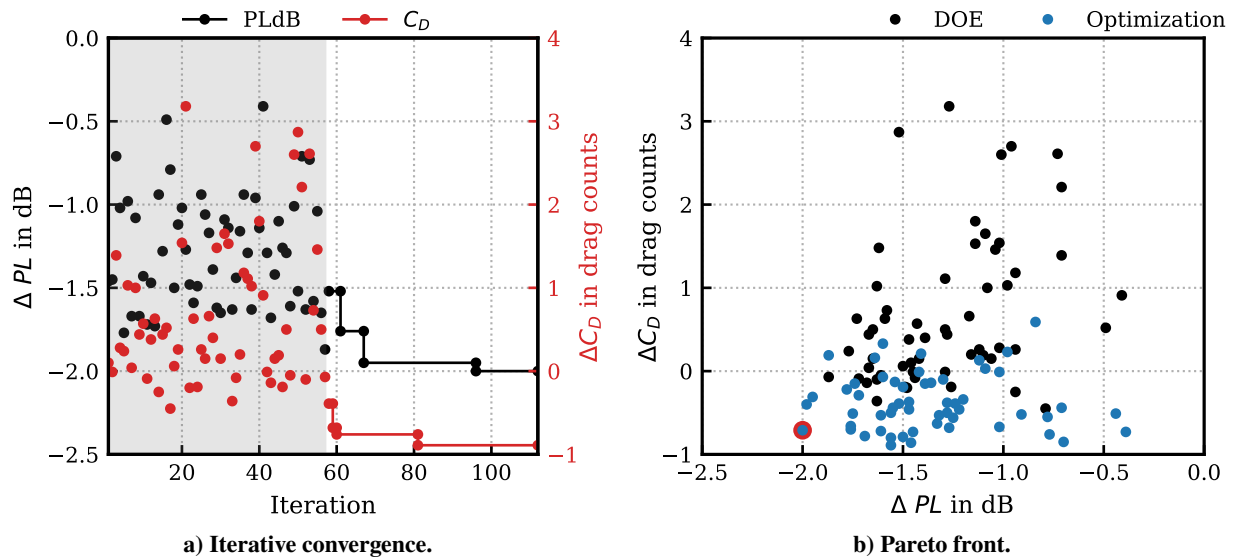

a) Iterative convergence.

b) Pareto front.

Fig. 7   Optimization iterations.

The optimization result will be called S4D4 O40-1 in the following sections. It is highlighted in Fig. 7b). The corresponding near-field signatures of the optimized nose configuration in comparison to the near-field signatures of the baseline geometry are shown in Fig. 8a) and Fig. 8b). Especially the relatively strong magnitudes of the shock and expansion pattern in the off-track signature at $X_N/L = 0.3$ were reduced. As a result, the off-track ground signature shown in Fig. 8d) is more rounded. As shown in Fig 8e), the maximum loudness occurring at 30° to 40° off-track angle was reduced by 2 dB PL. On the other hand, the on-track loudness was increased by 1 dB PL.
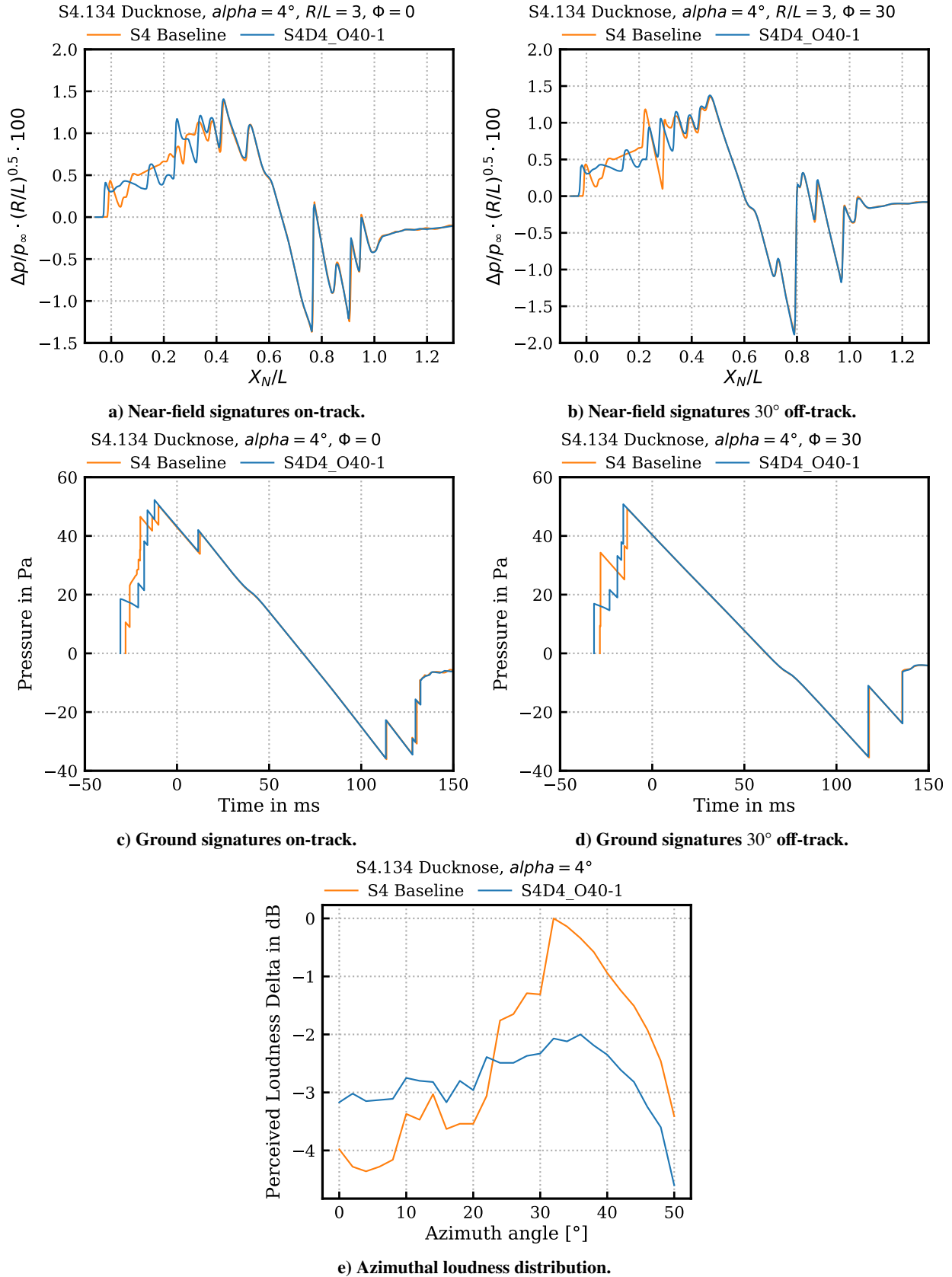
a) Near-field signatures on-track.

b) Near-field signatures 30° off-track.

c) Ground signatures on-track.

d) Ground signatures 30° off-track.

e) Azimuthal loudness distribution.

Fig. 8   Overview of the optimization of the aft part of the nose.

a) Front view.
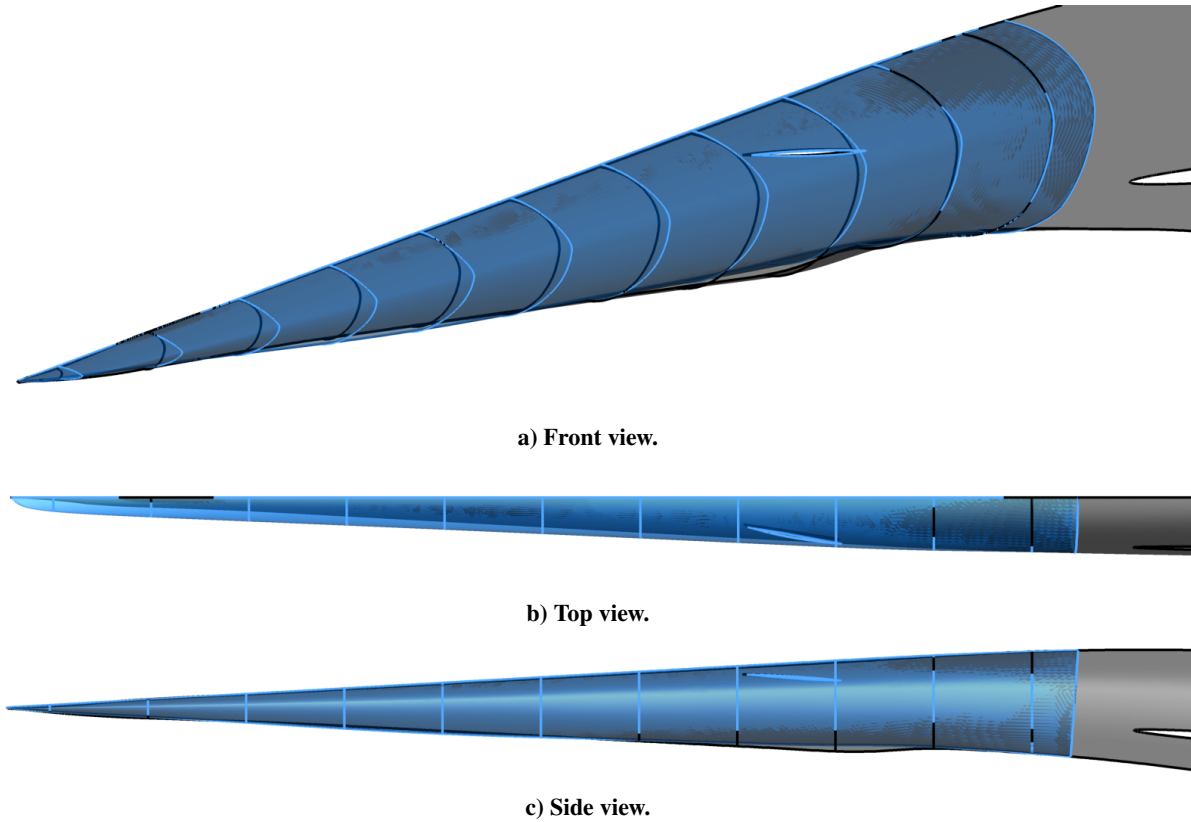

b) Top view.

c) Side view.

Fig. 9   Comparison of the geometries (black: S4.1.3.4th baseline, blue: S4D4_O40-1 optimized).

Figure 9 shows the comparison of the baseline (black) and optimized (blue) geometry. The width of the optimized nose shape is generally higher compared to the baseline S4.1.3.4th. However, the bump in fuselage height below the canard was significantly reduced. A similar result for a robust nose optimization with a reduced bump was published by Ueno and Makino in Ref. [1].
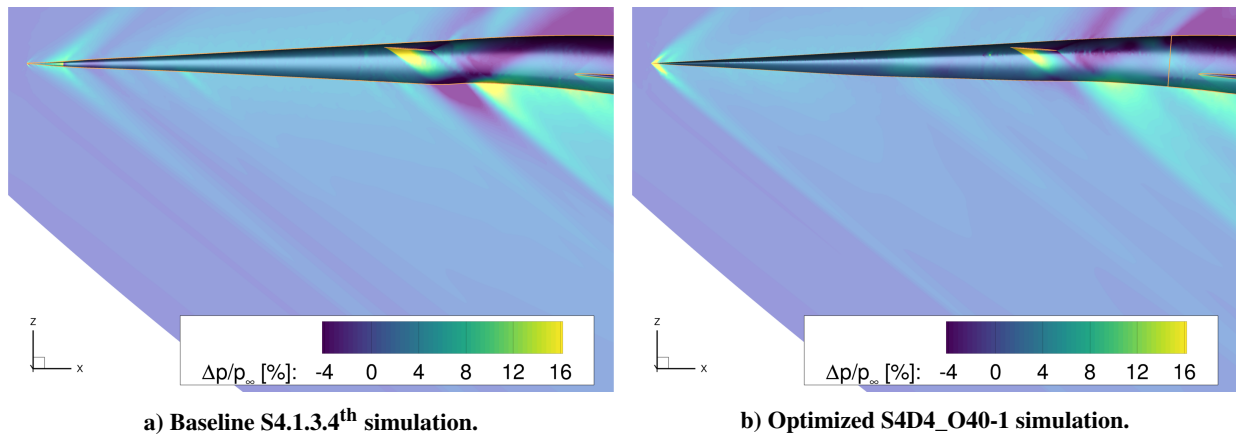

a) Baseline S4.1.3.4th simulation.

b) Optimized S4D4_O40-1 simulation.

Fig. 10   Overpressure on the symmetry plane.

A comparison of the pressure contours on the symmetry plane in shown in Fig. 10. The local pressure at the tip of the nose is increased by more than 20 % for the optimized case. The center of mass of the S4.1.3.4th is 44.1 m behind the nose [1]. Due to the large lever even small resulting forces at the nose could have an impact on the total pitching moment. Figure 11a) shows an analysis of the pitching moment plotted against the perceived loudness for this

optimization. No correlation between the pitching moment and the perceived loudness can be observed.

A deeper analysis of the contributions of the canard and the fuselage on the total pitching moment is shown in Figure 11b). It can be seen that the contribution of the fuselage is significantly lower than the contribution of the canard. However, this effect is still indirectly caused by the fuselage because the position of the canard is not centered in the fuselage. Thus, the increased width of the sections near the canard influences the lift from the canard and also the pitching moment. As a result, further trimming might be required.
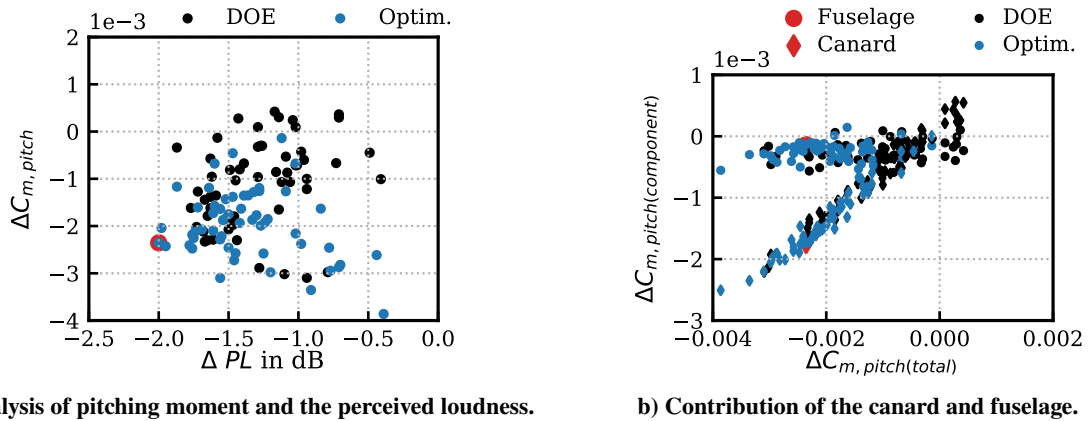

a) Analysis of pitching moment and the perceived loudness.

b) Contribution of the canard and fuselage.

Fig. 11   Analysis of the pitching moment.

IV. Summary and Outlook

In this paper a process for the multi-objective optimization of the nose of the JAXA S4.1.3.4[th] supersonic airliner was presented. The nose geometry was parameterized using a total of 16 design variables specifying the width and height at nine fuselage sections as well as the nose tip tangent angle. A modular grid setup for hybrid grids with a fully structured farfield for near-field pressure signature prediction was presented. A low-boom low-drag design was performed using inviscid simulations with the DLR TAU code. Both, the on-track and off-track loudness were considered within the optimization by using the maximum azimuthal loudness as second objective besides the drag coefficient.

The optimization was split into two steps. Initially the front part was shaped and finally the aft part. The front part of the nose has a significant impact on the perceived loudness while no significant influence on the drag coefficient was observed. This step resulted in a reduction of the perceived off-track loudness by up to 2 dB PL while increasing the on-track loudness by 1 dB PL and increasing the drag coefficient by two drag counts.

In the second step the aft part of the nose was optimized. The reduction of the maximal azimuthal loudness from the first step could be maintained while also reducing the drag coefficient by roughly one drag count compared to the baseline case.

The width of the nose was significantly increased compared to the baseline case while the bump in the fuselage below the canard was reduced. It was shown that the optimization had an indirect influence on the pitching moment by adding volume to the fuselage below the canard.

This highlights the importance of considering and accurately trimming the lift and the pitching moment within a low boom design process. Methods to adjust the trimming during CFD simulations using grid deformation are already available at DLR and should be applied in the future to account for varying pitching moments during the low boom design process. Furthermore, the widened nose of the optimized geometry results in increased surface area. RANS simulations should performed to analyze the impact of friction drag on the optimization result.

Acknowledgments

References

[1] Ueno, A., and Makino, Y., "Robust Low-Boom Design in Primary Boom Carpet," AIAA Paper 2021-1270, 2021. doi:10.2514/6.2021-1270.

[2] Park, M. A., and Nemec, M., "Near Field Summary and Statistical Analysis of the Second AIAA Sonic Boom Prediction Workshop," *AIAA Journal of Aircraft*, Vol. 56, No. 3, 2019, pp. 851–875. doi:10.2514/1.C034866.

[3] Rallabhandi, S. K., and Loubeau, A., "Propagation Summary and Statistical Analysis of the Second AIAA Sonic Boom Prediction Workshop," *AIAA Journal of Aircraft*, Vol. 56, No. 3, 2019, pp. 876–895. doi:10.2514/1.C034805.

[4] Carter, M. B., and Park, M. A., "Near Field Summary and Analysis of the Third AIAA Sonic Boom Prediction Workshop Shock-Plume Interaction Case," AIAA Paper 2021–469, 2021. doi:10.2514/6.2021-0469.

[5] Park, M. A., and Carter, M. B., "Nearfield Summary and Analysis of the Third AIAA Sonic Boom Prediction Workshop C608 Low Boom Demonstrator," AIAA Paper 2021–345, 2021. doi:10.2514/6.2021-0345.

[6] Rallabhandi, S. K., and Loubeau, A., "Summary of Propagation Cases of the Third AIAA Sonic Boom Prediction Workshop," AIAA Paper 2021–229, 2021. doi:10.2514/6.2021-0229.

[7] Kirz, J., and Rudnik, R., "DLR TAU Simulations for the Second AIAA Sonic Boom Prediction Workshop," *Journal of Aircraft*, Vol. 56, No. 3, 2019, pp. 912–927. doi:10.2514/1.C034819.

[8] Kirz, J., "DLR TAU Simulations for the Third AIAA Sonic Boom Prediction Workshop Near-Field Cases," AIAA Paper 2021–472, 2021. doi:10.2514/6.2021-0472.

[9] Carrier, G., Normand, P.-E., and Malbequi, P., "Analysis and Comparison of the Results of Two Tay Tracing-Based Sonic Boom Propagation Codes Applied to the SBPW3 Test Cases," AIAA Paper 2021–231, 2021. doi:10.2514/6.2021-0231.

[10] Ishikawa, H., Koganezawa, S., and Makino, Y., "Near Field Sonic Boom Simulations for C608 Airplane of the Third AIAA SPW by Unstructured/Structured Overset Grid Method," AIAA Paper 2021–346, 2021. doi:10.2514/6.2021-0346.

[11] Kirz, J., "Surrogate Based Shape Optimization of a Low Boom Axisymmetric Body," AIAA Paper 2018-2849, Jun. 2018. doi:10.2514/6.2018-2849.

[12] Kirz, J., "Surrogate Based Shape Optimization of a Low Boom Fuselage Wing Configuration," AIAA Paper 2019–3489, 2019. doi:10.2514/6.2019-3489.

[13] Liebhardt, B., Lütjens, K., Ueno, A., and Ishikawa, H., "JAXA's S4 Supersonic Low-Boom Airliner – A Collaborative Study on Aircraft Design, Sonic Boom Simulation, and Market Prospects," AIAA Paper 2020-2731, 2020. doi:10.2514/6.2020-2731.

[14] Ishikawa, H., Ueno, A., Koganezawa, S., Makino, Y., Liebhardt, B., and Lütjens, K., "Sensitivity Study and Primary Boom Carpet Assessment for Conceptual Low Boom Supersonic Transport," AIAA Paper 2021-0608, 2021. doi:10.2514/6.2021-0608.

[15] Ronzheimer, A., "CAD in Aerodynamic Aircraft Design,", No. DLRK 450117, 2017.

[16] Kirz, J., "Numerical Near-Field Simulations of Low Boom Aircraft Concepts," Deutscher Luft-und Raumfahrtkongress 2020 DocumentID 530263, 2020. doi:10.25967/530263.

[17] CentaurSoft, "CENTAUR - Mesh (Grid) Generation for CFD and Computational Simulations,", 2016. www.centaursoft.com [accessed 01 Dec. 2016].

[18] Schwamborn, D., Gerhold, T., and Heinrich, R., "The DLR TAU-Code: Recent Applications in Research and Industry," 2006. ECCOMAS CFD 2006: European Conference on Computational Fluid Dynamics.

[19] Wada, Y., and Liou, M.-S., "An accurate and robust flux splitting scheme for shock and contact discontinuities," *SIAM Journal on Scientific Computing*, Vol. 18, No. 3, 1997, pp. 633–657. doi:10.1137/S1064827595287626.

[20] Barth, T., and Jesperson, D., "The Design and Application of Upwind Schemes on Unstructured Meshes," AIAA Paper 1989–0366, Jan. 1989. doi:10.2514/6.1989-366.

[21] Taylor, A. D., "The TRAPS Sonic Boom Program," NOAA Technical Memorandum ERL–87, Jul. 1980.

[22] Wanner, J.-C. L., Vallee, J., Vivier, C., and Thery, C., "Theoretical and Experimental Studies of the Focus of Sonic Booms," *The Journal of the Acoustical Society of America*, Vol. 52, No. 1A, 1972, pp. 13–32. doi:10.1121/1.1913072.

[23] Wilke, G., "Variable-Fidelity Methodology for the Aerodynamic Optimization of Helicopter Rotors," *AIAA Journal*, 2019, pp. 1–14. doi:10.2514/1.J056486.

[24] Krige, D. G., "A statistical approach to some mine valuation and allied problems on the Witwatersrand," Ph.D. thesis, University of the Witwatersrand, 1951.

[25] Storn, R., and Price, K., "Differential Evolution–A simple and efficient heuristic for global optimization over continuous spaces," *Journal of Global Optimization*, Vol. 11, No. 4, 1997, pp. 341–359. doi:10.1023/A:1008202821328.

[26] Wilke, G. A., "Aerodynamic Optimization of Helicopter Rotor Blades using Variable Fidelity Methods," Ph.D. thesis, Technische Universität Carolo-Wilhelmina zu Braunschweig, November 2017.

[27] Ju, L., Du, Q., and Gunzburger, M., "Probabilistic methods for centroidal Voronoi tessellations and their parallel implementations," *Parallel Computing*, Vol. 28, No. 10, 2002, pp. 1477–1500. doi:10.1016/S0167-8191(02)00151-5.